GEOPHYSICS, VOL. 62, NO. 3 (MAY-JUNE 1997); P. 807–813, 4 FIGS.

Automatic conversion of magnetic data to depth, dip, and susceptibility contrast using the SPI (TM) method

Jeffrey B. Thurston* and Richard S. Smith*

ABSTRACT

The Source Parameter Imaging (SPI™) method computes source parameters from gridded magnetic data. The method assumes either a 2-D sloping contact or a 2-D dipping thin-sheet model and is based on the complex analytic signal. Solution grids show the edge locations, depths, dips, and susceptibility contrasts. The estimate of the depth is independent of the magnetic inclination, declination, dip, strike and any remanent magnetization; however, the dip and the susceptibility estimates do assume that there is no remanent magnetization. Image processing of the source-parameter grids enhances detail and provides maps that facilitate interpretation by nonspecialists.

The SPI method tests successfully on synthetic profile and gridded data. SPI maps derived from aeromagnetic data acquired over the Peace River Arch area of northwestern Canada correlate well with known basement structure and furthermore show that the Ksituan Magmatic Arc can be divided into several susceptibility subdomains.

INTRODUCTION

Magnetic data are used commonly to map thin magnetic sheets and/or contacts such as faults. An example of this is in petroleum exploration where magnetics is used to identify faults in the basement that may control the depositional history of the sedimentary basin. In this case, it is important that the interpreter has an understanding of the structural and lithological framework and the importance of regional deposition patterns. However, interpretation of the magnetics is complicated by:

1) the dipolar nature of the induced field;
2) possible offsets between the edges of the causative body and characteristic points on the response (peaks, crossovers);
3) asymmetric anomalies caused by a nonvertical magnetization direction, and
4) asymmetric anomalies caused by a nonvertical dip.

Thus, magnetic-data interpretation generally requires a specialist in potential-field methods who also has an excellent understanding of the geology.

There are a large number of methods designed to simplify magnetic data by removing one or more of the above complexities. Reduction to the pole (Baranov, 1957) removes the asymmetry caused by nonvertical magnetization direction, while the pseudogravimetric transform (Baranov, 1957) reduces a dipolar field to a monopolar field. Subsequently, the source edges are typically identified by a zero crossing on a second-vertical derivative profile or by maxima on a horizontal-gradient or analytic-signal amplitude profile. Sample profile plots of these quantities can be seen in Figure 1b. This example is a good illustration of how the zero crossing or maxima of the derivatives can be offset if the dip is nonvertical. The maximum of the analytic-signal amplitude, however, is independent of inclination, declination, remanent magnetization and dip—provided the sources are 2-D (i.e., have effectively infinite strike length). The disadvantage of the analytic-signal amplitude is that the mapped features are broad compared to the features on a second-vertical derivative map.

Another way of avoiding the above complications in the magnetic field and its subsequent transformations and derivatives is to deconvolve the total-field response into quantities that describe the causative body (the source parameters). This can be done manually for each anomaly using characteristic curves (e.g., Peters, 1949; Grant and West, 1965). Characteristic curves are still used widely (Spector and Lawler, 1995), as they do not require a computer, can be performed in the field, allow the user to differentiate between noise and signal, and can be applied to old analog data sets. Forward and inverse modeling methods are more sophisticated than characteristic curve techniques, but are usually more time consuming. Generally, these methods are not used on aeromagnetic surveys because of the large quantity of digital data now being collected.

Manuscript received by the Editor October 24, 1995; revised manuscript received August 28, 1996.
*Geoterrex, a Division of CGG Canada Ltd., 2060 Walkley Road, Ottawa, Ontario K1G 3P5, Canada.

Automatic source-parameter estimation can be accomplished either on a profile basis or on a grid basis. Profile techniques include the Naudy method (Naudy, 1971), Werner deconvolution (Hartman et al., 1971; Jain, 1976) and 2-D Euler deconvolution (Thompson, 1982). Such profile techniques assume a 2-D structure and that the structure is perpendicular to the flight line. In some cases, it may be possible to correct the result when these assumptions are not satisfied, but this is normally done manually, making it a time consuming task. Profile methods such as these are generally capable of estimating the depth, and in some cases, the magnetization, and the dip (assuming no remanence).

There are a number of methods that work on a grid; for example 3-D Euler deconvolution (Reid, 1990), the 3-D analytic-signal technique (Roest et al., 1992), and the enhanced analytic-signal technique (Hsu et al., 1996). The results from these methods are usually displayed by plotting a symbol at the interpreted source location; the size of the plotted symbol generally increases as the interpreted depth to the source increases. The advantage of grid methods is that they do not require profiles perpendicular to 2-D structures.

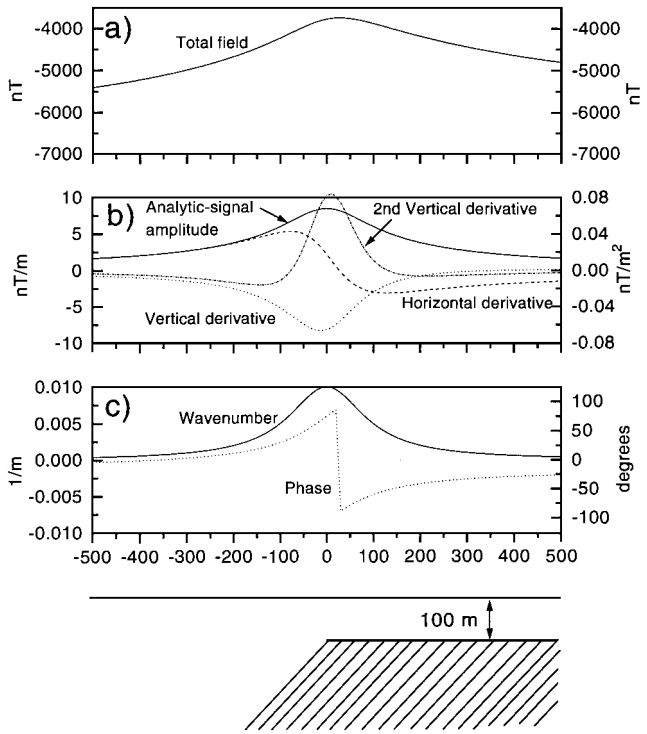

FIG. 1. (a) The total-field anomaly for the dipping contact model shown at the bottom of the figure. The dip is 135°, the depth to the top is 100 m, the ambient field strength is 60 000 nT, the susceptibility contrast is 0.01 SI, and the declination is zero degrees (for this particular model $2KFc\sin(d) = 848$ nT and $2I - d - 90 = -75°$). (b) Profiles of the analytic-signal amplitude, horizontal derivative, vertical derivative (all left axis) and the second-vertical derivative (right axis). Note that the horizontal derivative maximum and the second-vertical derivative zero crossing are both displaced from the top of the contact (zero). The analytic-signal amplitude peaks at zero, with a value of 8.48 nT/m. (c) The wavenumber and phase response. At $x = 0$, the wavenumber is 0.01 m^{-1}, and the phase is 75°. Using equations (11), (13), and (14), the local depth, the local dip, and the local susceptibility contrast are 100 m, 135°, and 0.01 SI, respectively.

We have developed a technique that works on gridded data, the results from which can be processed easily using off-the-shelf imaging processing software. One of our images can be used to determine the source location and the source depth. Unlike the second-vertical-derivative method, there is no offset of the estimated location (the cross-over) and the actual location. The image is not dipolar in nature and is independent of the magnetic inclination, the declination, the dip, the strike, and any remanent magnetization. Our only assumption is that the causative body is a 2-D contact or a thin sheet. If we also assume there is no remanent magnetization, it is possible to generate two additional images that show estimates of the dip and the susceptibility contrast.

Our goal is that these images can be interpreted by someone who is not familiar with magnetic data interpretation, but is an expert in the local geology.

METHODOLOGY

Our method extends the theory of the complex analytic signal (Nabighian, 1972, 1984; Atchuta Rao et al., 1981; Roest et al., 1992), by computing three complex attributes from which source parameters can be computed. In the analysis of temporal series these are: the instantaneous amplitude, analogous to the analytic-signal amplitude computed by Roest et al. (1992); the instantaneous phase; and, the instantaneous frequency (see e.g., Taner et al., 1979). Prefacing the attribute name with instantaneous makes the distinction clear between these quantities and their spectral namesakes. As magnetic data are spatial, rather than temporal, we use the term *local* instead of instantaneous.

The use of the complex analytic signal, which assumes 2-D sources, has two additional appealing features. First, this complex function can be computed for either total-field or horizontal-gradient data. The former case is used for source-parameter estimation assuming a thin-sheet model, while the latter case is for sources that are assumed to be sloping contacts with effectively infinite depth extent. Thus, the assumed model can be altered by changing only the quantity that is input to the algorithm. Further, use of the complex analytic signal means that depth can be computed without a priori knowledge of the magnetization direction. As with other automatic methods, there is no easy way of determining which model is most appropriate.

Complex attributes

Nabighian (1972) defined the complex analytic signal in two ways: (1) in terms of the horizontal and vertical derivatives and (2) in terms of the total field and its Hilbert transform. The former definition is

$$A(x,z) = \frac{\partial M(x,z)}{\partial x} - j\frac{\partial M(x,z)}{\partial z}, \qquad (1)$$

where $M(x,z)$ is the magnitude of the total magnetic field, j is the imaginary number, z and x are Cartesian coordinates for the vertical direction and the direction perpendicular to strike. Equation (1) is equivalent to

$$A(x,z) = |A|\exp(j\theta), \qquad (2)$$

where

$$|A| = \sqrt{\left(\frac{\partial M}{\partial x}\right)^2 + \left(\frac{\partial M}{\partial z}\right)^2}, \tag{3}$$

and

$$\theta = \tan^{-1}\left[\frac{\partial M}{\partial z} \Big/ \frac{\partial M}{\partial x}\right]. \tag{4}$$

By definition, the analytic-signal amplitude and the local phase are given in equations (3) and (4), respectively (see e.g., Bracewell, 1965). Atchuta Rao et al. (1981) have described a manual source-parameter estimation process that works on a profile basis and uses the analytic-signal amplitude and phase. Our method also uses the local frequency, denoted f, which is defined as the rate of change of the local phase with respect to x (Bracewell, 1965). This quantity is given by

$$f = \frac{1}{2\pi}\frac{\partial}{\partial x}\tan^{-1}\left[\frac{\partial M}{\partial z} \Big/ \frac{\partial M}{\partial x}\right]. \tag{5}$$

In the analysis of potential fields, it is often more convenient to use local wavenumber, denoted by κ, rather than f where

$$\kappa = 2\pi f. \tag{6}$$

Making this substitution, and using the differentiation rule $d(\tan^{-1}\phi)/dx = 1/(1+\phi^2)$ gives

$$\kappa = \frac{1}{|A|^2}\left(\frac{\partial^2 M}{\partial x \partial z}\frac{\partial M}{\partial x} - \frac{\partial^2 M}{\partial x^2}\frac{\partial M}{\partial z}\right). \tag{7}$$

Complex attributes can also be computed for the analytic signal of the thin-sheet model. This is done by replacing the horizontal gradient in the real part of equation (1) with the total-magnetic field, and the vertical gradient in the imaginary part with the Hilbert transform of the total-magnetic field.

Source-parameter estimation

We now show how the complex attributes can be used directly to determine the edge location, depth, dip, and susceptibility contrast. We begin with the expressions for the vertical and horizontal gradients of a sloping contact

$$\frac{\partial M}{\partial z} = 2KFc\sin d \times \frac{x\cos(2I-d-90) - h\sin(2I-d-90)}{h^2+x^2}, \tag{8}$$

$$\frac{\partial M}{\partial x} = 2KFc\sin d \times \frac{h\cos(2I-d-90) + x\sin(2I-d-90)}{h^2+x^2}, \tag{9}$$

(Nabighian, 1972), where K is the susceptibility contrast at the contact, F is the magnitude of the Earth's magnetic field, $c = 1 - \cos^2 i \sin^2\alpha$, α is the angle between the positive x-axis and magnetic north, i is the ambient-field inclination, $\tan I = \tan i/\cos\alpha$, d is the dip (measured from the positive x-axis), h is the depth to the top of the contact and all trigonometric arguments are in degrees. Substituting equations (8) and (9) into the expression for the local wavenumber (7) yields

$$\kappa = \frac{h}{h^2+x^2}, \tag{10}$$

where the coordinate system has been defined such that $x = 0$ directly over the edge. Equation (10) makes it evident that maxima of the local wavenumber are independent of the magnetization direction. Thus, the peaks outline source edges, and at these locations $x = 0$. At $x = 0$, we can calculate "local depth" defined by

$$h = \frac{1}{\kappa}. \tag{11}$$

To compute the "local dip," denoted d, expressions for the gradients of the sloping contact are substituted into the expression for the local phase [equation (4)], giving

$$\theta = \tan^{-1}\left(\frac{x\cos(2I-d-90) - h\sin(2I-d-90)}{h\cos(2I-d-90) + x\sin(2I-d-90)}\right). \tag{12}$$

The local dip can be estimated by setting $x = 0$ and rearranging equation (12) to give

$$d = \theta + 2I - 90. \tag{13}$$

In deriving equation (13), and in the following, we assume no remanent magnetization. Finally, the "local susceptibility" is given by setting $x = 0$ and substituting equations (8) and (9) into equation (3). If the local depth and local dip are used in place of depth and dip, respectively, then

$$K = \frac{|A|}{2\kappa Fc\sin d}. \tag{14}$$

Equations (13) and (14) give the local dip and local susceptibility contrast only at the source boundaries ($x = 0$). Because these functions are not necessarily extrema at these locations, it is necessary first to determine the edge positions from the maxima of the local wavenumber.

As an example of the usefulness of these quantities, we have plotted the wavenumber, and the phase on Figure 1c. Clearly, the peak in the local wavenumber represents the contact position, where $x = 0$. Using the wavenumber, the phase and the analytic-signal amplitude at this position, the local depth, the local dip and the local susceptibility contrast can be derived as 100 m, 135°, and 0.01 SI, respectively. These quantities all agree exactly with the source parameters used in generating the synthetic data.

In the derivation of the local depth, dip, and susceptibility, it has been assumed that there is no interference from adjacent anomalies. This type of interference corrupts the results from all automatic algorithms and generally requires that detailed modeling be used for an accurate quantitative analysis. Hartman et al. (1971) discuss a method for dealing with interference on a profile basis. However, since we are calculating second-order derivatives to generate the images, the interference will be much less than if we were using total-field or first-derivative data.

For the thin sheet model, the total field and its Hilbert transform are given by the right-hand sides of equations (9) and (8), respectively (Reford, 1964; Nabighian, 1972). The only

difference is that the susceptibility contrast (K) is replaced by the susceptibility-thickness (kw). With this substitution, all subsequent equations are identical.

Source-parameter imaging

Estimation of source parameters can be performed on gridded magnetic data. This has two advantages. First, this eliminates errors caused by survey lines that are not oriented perpendicular to strike. Second, there is no dependence on a user-selected window or operator size, which other techniques like the Naudy and Euler methods require. In addition, grids of the output quantities can be generated, and subsequently image processed to enhance detail and provide structural information that otherwise may not be evident.

In practice, we have accomplished this on gridded data by estimating the strike direction at each grid point. We calculate the vertical gradient in the frequency domain, and the horizontal derivatives are computed in the direction perpendicular to strike using the least-squares method of Thurston and Brown (1994). The problem therefore reduces to that described in equations (1) through (14) above.

The effectiveness of the method can be demonstrated on synthetic gridded data. The model used is a parallelepiped 2500×2500 m, buried 500 m, and with a depth extent of 20 km. The susceptibility contrast of the model with the surrounding medium is 0.13 SI units. The total field is shown in Figure 2a and the analytic-signal amplitude, calculated using the method in Roest et al. (1992), is shown on Figure 2b. The maxima of the analytic-signal amplitude outlines the vertical projection of the edges of the body (these edges are at an angle of 20° to the cardinal points of the compass). Along the southern edge, the peak is diffuse, making it difficult to identify edge locations and to estimate the source depths using the half width of the analytic-signal-amplitude anomaly (Nabighian, 1972; Roest et al., 1992). By contrast, the peaks of the local wavenumber (Figure 1c), which are defined by the hotter colors, are resolved more sharply. The color bar of Figure 1c has been labeled with the inverse of the local wavenumber, so the depth can be read off the image at the peak position. Using image processing algorithms, it is also possible to display the inverse of the local wavenumber only at the position where the local wavenumber is a maximum, thereby generating a map on which all points that are not null represent contact positions and the colors give an indication of the depth of the contacts. This is what is displayed on the local depth map (Figure 2d). The depths derived in this fashion are about 500 m (the true value), except along the north edge, where the estimated depths are about 700 m. These poorer solutions occur where the total-field image (Figure 2a) shows significant curvature and our assumption of two dimensionality is somewhat violated. For this example, the images of local dip and local susceptibility contrast (also plotted where the wavenumber is a maximum) give answers close to the true values of 90° and 0.13 SI units, respectively. For this example, the maximum variation from the true value is about 20° for the dip and a factor or two for the susceptibility contrast. Again, the poorer estimates of local dip and susceptibility contrast are where the data are not 2-D. At present, the algorithm is not able to determine whether or not the sources are adhering to the assumption of two-dimensionality. This decision is currently left to the interpreter.

FIELD DATA AND DISCUSSION

We demonstrate this technique on nonexclusive data that are part of a larger survey flown by Geoterrex in 1989. These data were acquired with the intention of mapping Precambrian basement underlying the sedimentary section in northwestern Alberta and northeastern British Columbia. Tests conducted prior to the survey revealed that a constant barometric elevation of 1200 m above sea level suppressed the majority of the cultural effects, and still provided good resolution of basement anomalies. The lines are oriented north-south, at a spacing of 1.6 km, and the tie-lines are spaced at 4.8 km. Diurnal variations have been removed with a standard line/tie-line leveling procedure, the IGRF has been subtracted, and the total field has been gridded at an interval of 250 m. These data are shown in Figure 3a. For reference, the Ksituan Magmatic Arc, as interpreted in Ross et al. (1991), is labeled on this map.

Source-parameter images have been generated for this data set assuming the sources to be sloping contacts. Compared with the analytic-signal amplitude (3b), there is greater resolution in the local-wavenumber image (3c). Thus, we present the local wavenumber as an alternative to the analytic signal amplitude as both have the appealing feature of being independent of the ambient field direction and the dip, but the local wavenumber provides greater resolution and has maxima that are inversely proportional to depth.

Once the maxima of the local wavenumber are determined, we can image the local depth, local dip, and local susceptibility contrast along the contacts (Figures 4a, 4b and 4c). The interpretation of these images is aided by superimposing the local depth, dip, and susceptibility contrast (as color) over a grey-scale image of the sun-illuminated total field.

From these images, an interpreter can recognize variations that may occur along strike. Note, for example, the depth variation along the Dunvegan Fault (the linear feature that forms the southeastern boundary of the Ksituan Magmatic Arc). Crude contouring of the well-log information indicates that the top of the basement occurs at about 2 km below sea level along the southeastern edge of the Ksituan Arc (Cant, 1988). The depths from the source-parameter images indicate the sources that are 2-D are deeper than 3.3 km below the sensor, which corresponds to more than 2.1 km below sea level (which is within the basement). Further, the depth image correlates with variations between known blocks in the basement. To demonstrate this we have overlain (on Figure 4a) the trace of a horst and graben system (the Axial Graben; Cant, 1988) that underlies the axis of the Peace River Arch. The uplifted portion of the basement corresponds to relatively shallow estimated depths (redder), while the adjacent basement lows correspond to deeper depths (greener). Additional structural information is provided by the local-dip image: Figure 4b indicates that most of the coherent 2-D features that comprise the Ksituan Domain are near vertical. This near-vertical structure is consistent with statements made in Zelt and Ellis (1989), indicating that our assumption of no remanent magnetization in this area is reasonably well satisfied.

Unfortunately, a paucity of basement lithological data precludes detailed ground truthing of the local susceptibility contrast estimates (Figure 4c). However, we can use this image to draw new conclusions about the Ksituan Magmatic Arc.

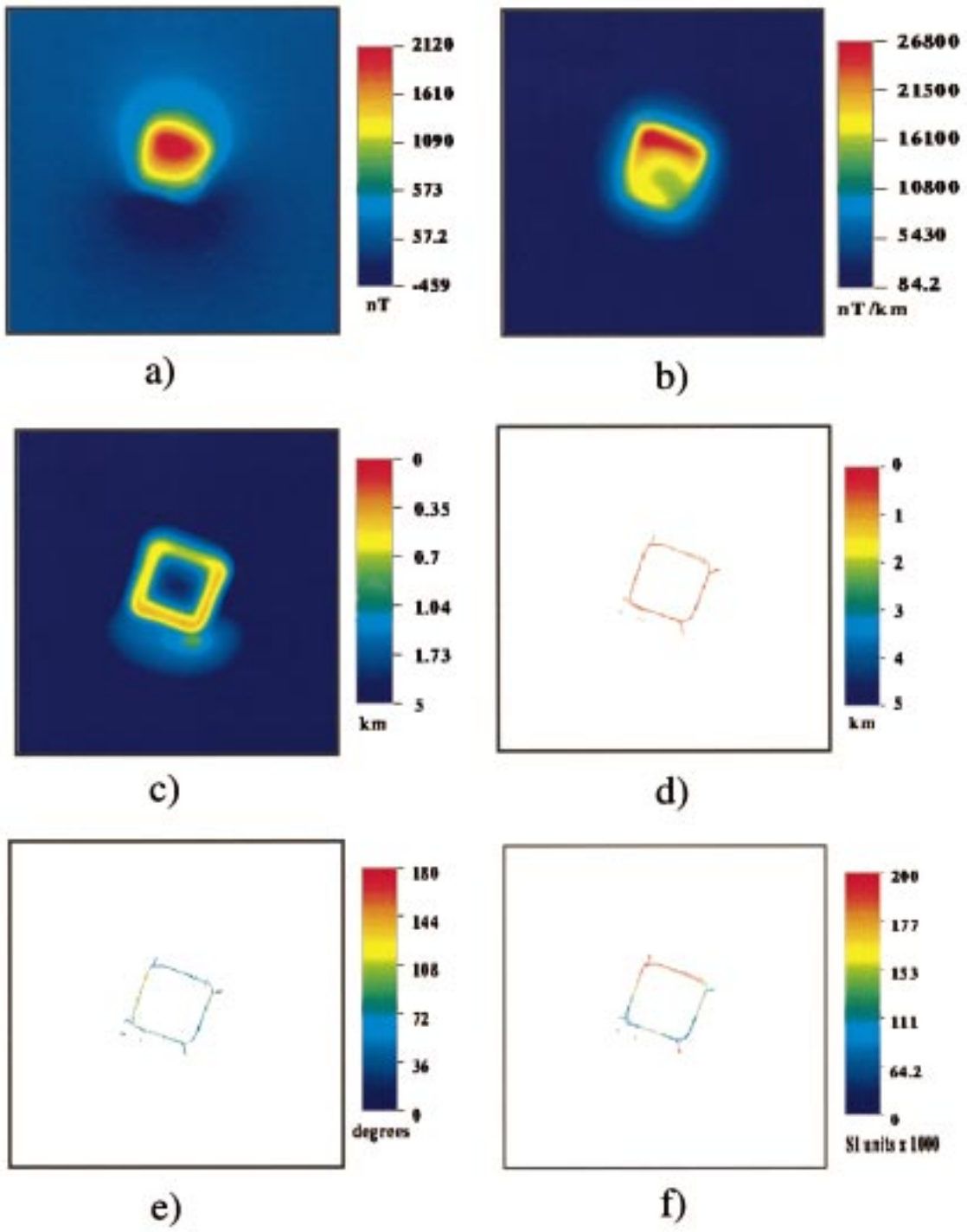

FIG. 2. (a) The total magnetic anomaly of a synthetic parallelepiped model 2500 m by 2500 m, with a depth to top of 500 m, and a depth to bottom of 20 km. The sides of the model are vertical, but are oriented 20° to the east of grid (and magnetic) north. In SI units, the susceptibility contrast at the edge is 0.13. The Earth's magnetic field has an inclination of −61° (southern hemisphere), a declination of zero, and a field strength of 56 000 nT. The map area shown is 12.8 km square and geographic north is to the top of the figure. (b) The image of the analytic-signal amplitude (assuming a contact model). The peaks of the analytic-signal define the contacts (or edges) of the block. Note that the peak is diffuse on the southern edge of the body. (c) The inverse of the local wavenumber, the peak position of which also defines the edges of the block. On this image, hot colors represent large local wavenumbers or small inverse local wavenumbers. The color bar is labeled with the inverse local wavenumber. (d) The local depth, which is the inverse of the local wavenumber. The only positions imaged are those where the local wavenumber peaks, where we assume that $x = 0$. (e) The local dip of the contact. Contacts with a component of dip to the east have dips in the range zero to 90° (vertical) and dips to the west are in the range 90° to 180°. (f) The apparent susceptibility contrast at the contact. The estimates of local depth, dip, and susceptibility contrast assume the data are 2-D (no variation along strike). The extent to which the violation of this assumption affects the results can be seen on the northern edge, where the magnetic-field image shows significant curvature and is thus not 2-D.

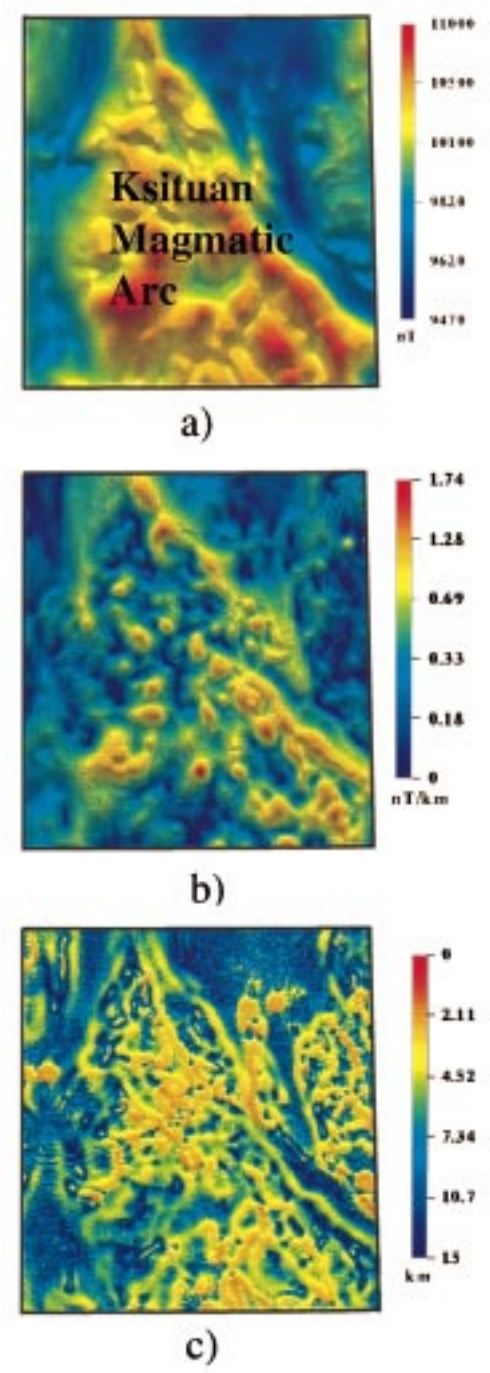

FIG. 3. (a) The total magnetic field, (IGRF) removed, for an area in the Western Canadian Sedimentary Basin that is approximately 160 × 160 km. The sensor is 1.2 km above sea-level and geographic north is to the top of the figure. (b) The analytic-signal amplitude of Roest et al. (1992), which implicitly assumes a contact model. (c) The local wavenumber: warm colors indicate high wavenumber, cool colors low wavenumber. The color bar has been labeled with the inverse of the local wavenumber so it has units of km. This image is particularly useful for extracting structural information as it has been enhanced with a sun-angle illumination. At a peak in the local wavenumber ($x = 0$), the inverse of the local wavenumber will correspond to the depth of the contact below the sensor. The peaks of the analytic-signal amplitude and the local wavenumber can both be used to map the contacts or edges of magnetic bodies. However, the local wavenumber corresponds to a higher derivative and thus shows more features and greater resolution.

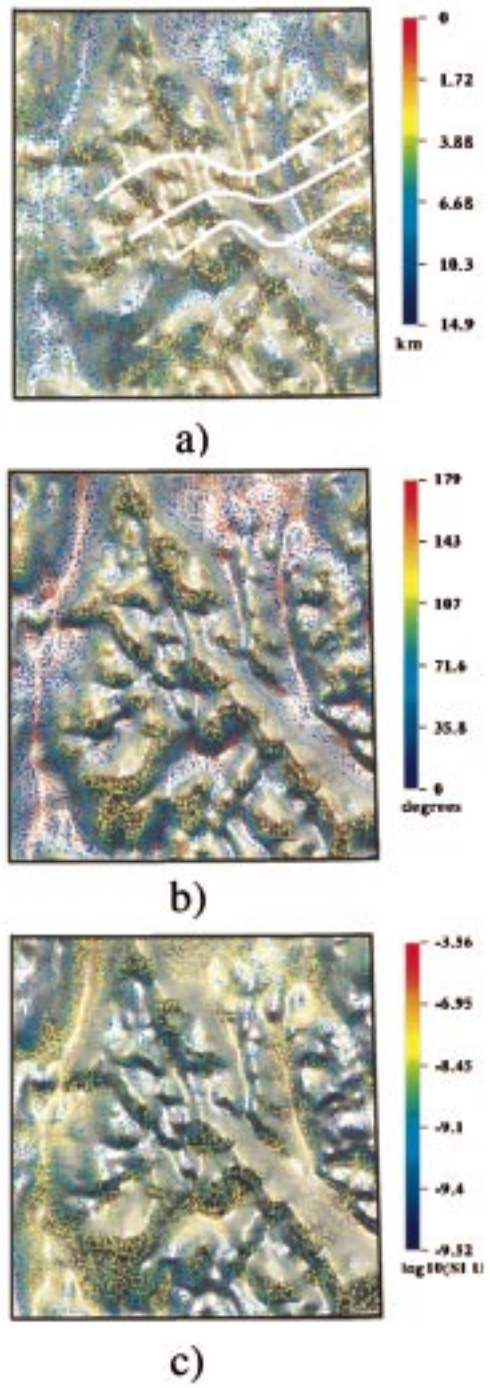

FIG. 4. (a) The estimated local depth for the same area as Figure 3. This depth (below the sensor) is shown in color at the contact position and has been superimposed on a greyscale image of the magnetic shaded relief. The white lines on the image represent faults, interpreted from existing well-log data in Cant (1988). They show a horst and graben system following the Peace River Arch. The down-thrown side is indicated by the small tick marks. (b) The estimate of the local dip of the contacts. Contacts with a component of dip to the east are cool colors (blue is 0° dip), vertical dips are yellow, and westerly dips are hot colors (red is 180° dip). (c) The estimate of the local susceptibility contrast at the contact. The range of the local susceptibility contrast is compressed using the common logarithm. The local depth, dip, and susceptibility contrast are only plotted at the peak of the local wavenumber, where we assume that $x = 0$. The local susceptibility contrast and local dip maps assume there is no remanent magnetization.

The image shows that the Arc is not necessarily homogeneous (Ross et al., 1991), it can be subdivided further into several subdomains on the basis of the variation in the susceptibility contrast.

CONCLUSION

Automatic estimation of the source parameters can be done rapidly and easily. The estimates are independent of the magnetic inclination and free from effects associated with the dipolar nature of the magnetic response. The local wavenumber map more closely resembles the geology than the total-field magnetic map and its derivatives. Correct estimates of the source parameters are only obtained when the structure is 2-D and corresponds to the chosen model (sloping contact or dipping thin sheet). The estimates of dip and susceptibility are only reliable if the remanent magnetization is small.

The estimates of source parameters we obtain from the images are consistent with the known source information (for the synthetic data) and the known geological information (for the field data). Furthermore, in the field example we obtained additional information that extends our understanding of this geologically complex area considerably.

The images presented can be interpreted easily by a non-specialist familiar with the local geology and the current exploration concepts. There is no requirement for a detailed understanding of the principles of magnetic data interpretation or a knowledge of the technicalities of the source-parameter estimation algorithm.

ACKNOWLEDGMENTS

The authors would like to thank GEOTERREX, a Division of CGG Canada Ltd., for permission to publish images of a portion of the nonexclusive data set from western Canada. Dave Daggar kindly generated the synthetic data shown in Figure 2 and assisted us with the imaging processing algorithms. We would like to thank David A. Chapin, Afif H. Saad and Harold L. Yarger for constructive reviews that greatly improved the quality of the manuscript. Source Parameter Imaging and SPI are trademarks of Geoterrex.

REFERENCES

Atchuta Rao, D., Ram Babu, H. V., and Sanker Narayan, P. V., 1981, Interpretation of magnetic anomalies due to dikes: The complex gradient method: Geophysics, **46**, 1572–1578.

Baranov, V., 1957, A new method for interpretation of aeromagnetic maps: pseudo-gravimetric anomalies: Geophysics, **22**, 359–383.

Bracewell, R., 1965, The Fourier transform and its applications: McGraw-Hill Book Co.

Cant, D. J., 1988, Regional structure and development of the Peace River Arch, Alberta: A Paleozoic failed-rift system? Bull. Can. Petr. Geol., **36**, 284–295.

Grant, F. S., and West, G. F., 1965, Interpretation theory in applied geophysics: McGraw Hill Book Co.

Hartman, R. R., Teskey, D. J., and Friedberg, J. L., 1971, A system for rapid digital aeromagnetic interpretation: Geophysics, **36**, 891–918.

Hsu, S.-K., Sibuet, J.-C., and Shyu C.-T., 1996, High-resolution detection of geologic boundaries from potential-field anomalies: An enhanced analytic signal technique: Geophysics, **61**, 373–386.

Jain, S., 1976, An automatic method of direct interpretation of magnetic profiles: Geophysics, **41**, 531–541.

Nabighian, M. N., 1972, The analytic signal of two-dimensional magnetic bodies with polygonal cross-section: Its properties and use for automated anomaly interpretation: Geophysics, **37**, 507–517.

———1984, Toward a three-dimensional automatic interpretation of potential-field data via generalized Hilbert transforms: Fundamental relations: Geophysics, **49**, 780–786.

Naudy, H., 1971, Automatic determination of depth on aeromagnetic profiles: Geophysics, **36**, 712–722.

Peters, L. J., 1949, The direct approach to magnetic interpretation and its practical application: Geophysics, **14**, 290–320.

Reid, A. B., Allsop, J. M., Granser, H., Millet, A. J., and Somerton, I. W., 1990, Magnetic interpretation in three dimensions using Euler deconvolution: Geophysics, **55**, 80–91.

Reford, M. S., 1964, Magnetic anomalies over thin sheets: Geophysics, **29**, 532–536.

Roest, W. R., Verhoef, J., and Pilkington, M., 1992, Magnetic interpretation using the 3-D analytic signal: Geophysics, **57**, 116–125.

Ross, G. M., Parrish, R. R., Villeneuve, M. E., and Bowring, S. A., 1991, Geophysics and geochronology of the crystalline basement of the Alberta Basin, western Canada: Can. J. Earth Sci., **28**, 512–522.

Spector, A., and Lawler, T. L., 1995, Application of aeromagnetic data to mineral potential evaluation in Minnesota: Geophysics, **60**, 1704–1714.

Taner, M. T., Koehler, F., and Sheriff, R. E., 1979, Complex seismic trace analysis: Geophysics, **44**, 1041–1063.

Thompson, D. T., 1982, EULDPH: A new technique for making computer-assisted depth estimates from magnetic data: Geophysics, **47**, 31–37.

Thurston, J. B., and Brown, R. J., 1994, Automated source-edge location with a new variable pass-band horizontal-gradient operator: Geophysics, **59**, 546–554.

Zelt, C. A., and Ellis, R. M., 1989, Seismic structure of the crust and upper mantle in the Peace River Arch region, Canada: J. Geophys. Res., **94**, No. B5, 5729–5744.